# A Perturbation Observer-Based Fast Frequency Support Control for Low-Inertia Power Grids Through VSC-HVDC Systems

Weiyu Wang, *Member, IEEE*, Yijia Cao, *Senior Member, IEEE*, Lin Jiang, *Member, IEEE*, Chun Chen, *Member, IEEE*, Yong Li, *Senior Member, IEEE*, Shuaihu Li, *Member, IEEE*, Xingyu Shi, *Member, IEEE*

***Abstract*—Low-inertia power grids could suffer from large frequency excursions under even small power disturbances. When a voltage source converter-based high voltage direct current (VSC-HVDC) system is used to integrate a low-inertia grid into a main grid, an ancillary frequency support service can be provided to the low-inertia grid by the VSC-HVDC system. This paper proposes a perturbation observer-based fast frequency support controller (POFFS) of VSC-HVDC systems to improve the frequency stability of low-inertia power grids. According to the feedback linearization and the high gain observer technique, the perturbation observer of the inverter station is designed to estimate the comprehensive impact of multiple perturbations, including the power disturbances in low-inertia grids, the uncertainty of grid inertia, and unknown nonlinear dynamics. The estimate of the perturbations are further compensated by the feedback control loop to achieve robust frequency regulation. Compared with the conventional frequency controller, the proposed POFFS can provide better frequency support to low-inertia power grids, without requiring an accurate system model and parameters. Two test systems are used to verify the effectiveness of the proposed POFFS.**

***Index Terms*—VSC-HVDC, low-inertia grid, frequency support, feedback linearization, perturbation observer.**

## I. Introduction

VOLTAGE Source Converter based High Voltage Direct Current System (VSC-HVDC) is considered to be a flexible and economic solution to transmit bulk power over long distances [1]. Owing to the decoupling interconnection capability, asynchronous ac grids can be connected via VSC-HVDC systems without the concern of synchronization issues.

Although the asynchronous interconnection through VSC-HVDC can prevent the spread of faults between ac grids, it also raises new challenges in frequency regulation from three aspects. The first aspect is that the grid inertia could be reduced since the proportion of power generation from synchronous generators (SG) decreases. Another reason is that VSC-HVDC systems hinder the inherent power support between ac grids. The disturbed ac grid can only rely on its power reserve to regulate frequency. Moreover, the uncertainties introduced by renewable energies would place much burden on maintaining the supply-demand balance. Hence, for low inertia power systems, the power deficiency would result in a large frequency deviation [2]. For example, in 2019, the UK suffered from a widespread blackout due to the severe frequency deviation, which was caused by the sudden outage of gas generators and wind generators under a low inertia operating state [3].

To improve frequency stability, ancillary frequency service can be designed for VSC-HVDC systems, which have several superior advantages in power regulation [4], including the independent control of active and reactive power, fast reference tracking, and flexible power reversal ability. Thus, the power deficiency of ac grids could be compensated promptly by regulating the active power output of VSC stations to restrain the frequency excursion.

In the past decade, many researchers have investigated the design of ancillary frequency support controllers of VSC-HVDC systems. The basic idea of frequency support via HVDC links is imitating the droop characteristic of the speed-governor of SGs, i.e., the primary frequency regulation (PFR) or $P-\omega$ droop control, which changes the active power reference of converters with the grid frequency deviation [5]–[11]. The advantage of PFR is that the power deficiency in ac grids can be proportionately shared between VSC stations and SGs by setting the droop gain. In [5], [6], communication-free control strategies are proposed to coordinate wind farms and HVDC-links to provide primary frequency support to ac grids. The grid frequency fluctuation signal is converted into the dc voltage variation, which could be captured by wind farms and further activate the inertia response function. To deal with the second frequency drop issue caused by the inertia response of wind farms, an adaptive droop control strategy is investigated in [7], which can dynamically change the droop gains at different frequency recovery stages.

Considering multiple asynchronous ac grids connected by multi-terminal HVDC systems, Ye et al. [8] proposed a cross-regional power flow control method to provide frequency support by sharing the power reserves among asynchronous ac grids, and Wang et al. [9] proposed a consensus protocol-

This work was supported by Hunan Provincial Natural Science Foundation of China (2021JJ40598), Scientific Research Fund of Hunan Provincial Education Department (21B0325), and the National Natural Science Foundation of China under Grant (51777179). (Corresponding authors: Chun Chen, and Yijia Cao.)

W. Wang, Y. Cao, C. Chen, S. Li, and X. Shi are with the School of Electrical and Information Engineering, Changsha University of Science and Technology, Changsha 410114, China. (e-mail: WYWang@csust.edu.cn, yjcao@csust.edu.cn, chch3266@126.com, lishuaihu2010@126.com, sxywd0602@hnu.edu.cn).

L. Jiang is with the Department of Electrical Engineering and Electronics, University of Liverpool, Liverpool L69 3GJ, U.K. (e-mail: ljiang@liv.ac.uk).

Y. Li is with the College of Electrical and Information Engineering, Hunan University, Changsha 410082, China. (e-mail: yongli@hnu.edu.cn).

based control strategy to improve the frequency stability and minimize the dc voltage deviation. To find the most suitable converter to provide inertia and frequency support, a selective power routing method and model predictive controller are developed in [10]. In [11], the inertia and PFR are synthesized to improve the frequency stability through VSC-HVDC systems. However, PFR is essentially a proportional controller, which cannot eliminate the steady-state frequency deviation even if the converter station has available head room.

In recent years, grid-forming control (GFC) has drawn much attention in the field of frequency regulation. GFCs can provide inertia support and PFR through inverters by emulating the dynamics of synchronous generators (SG) [12]. Multiple types of GFCs have been developed and have achieved the satisfying performance on inertia and frequency support [13], e.g., virtual synchronous generator (VSG), frequency-power droop control with low-pass filter, power-synchronization control, etc. Owing to similar dynamic characteristics with SGs, GFCs could interact with SGs in a low-frequency and subsynchronous-frequency range [14]–[16]. Consequently, the dynamics of hybrid ac/dc systems become more complicated when GFCs are adopted, and the controller parameters must be carefully tuned to avoid transient instability issues [17].

To achieve zero frequency error and to fully utilize the capability of the inverter station, a natural idea is to use the integral controller or the proportional-integral (PI) controller to continually adjust the power output of inverters to restore the frequency to the nominal value. In [18] and [19], the conventional PI controller is used to regulate the grid frequency in VSC-HVDC systems and LCC-VSC hybrid systems. Since the frequency measurement is often obtained from the transmission system operator (TSO), the impact of communication delay on system stability must be considered during frequency regulation. A delay margin estimate method is proposed in [20] to guide the setting of controller parameters. With the inspiration of this approach, more advanced control techniques are used to design the delay-dependent PI-based frequency controller to attenuate the negative effect of the communication delay, e.g., Linear matrix inequality (LMI), Lyapunov theory and event-triggering techniques [21]–[23]. However, the tuning process of PI-based controllers rely on the knowledge of the control plant whilst the model errors and parameter uncertainties are inevitable in real applications, which could deteriorate the performance of PI-based controllers [24].

To obtain reliable frequency support performance with disturbances, two types of robust control techniques can be adopted. One type is based on the robust control theory, e.g., $H\infty$ and $\mu$ synthesis control techniques, which can mitigate the impact of uncertainties on system dynamics by limiting the gain from input disturbance to measured output [25]–[27]. The other one is based on the concept of active disturbance rejection control (ADRC) or perturbation observer-based control (POC). Multiple disturbances can be regarded as a lumped perturbation term, which can be estimated by observers and be compensated through feedback controllers [24], [28]–[30]. Hence, better robustness and tracking accuracy can be obtained by POC.

Originating from the concept of POC, this paper proposes a perturbation observer-based fast frequency support (POFFS) controller for VSC-HVDC systems, which is composed of a perturbation observer and an output feedback controller. The perturbation observer aims at estimating the comprehensive effect of multiple disturbances on grid frequency, and the feedback controller is designed to compensate the impact of disturbances on system dynamics in real-time and to achieve the optimal frequency regulation. The performance of the proposed controller is verified by two case studies in DIgSILENT/PowerFactory. The contributions of this paper can be summarized as follows:

1) The inverter station of the VSC-HVDC system and the adjacent ac grid are treated as a whole control plant, and the nonlinear relationship between the power reference of the inverter station and the grid frequency is derived. The original nonlinear model is transformed into an equivalent input-output linear system, which is further used for the design of the perturbation observer.
2) A lumped perturbation term is defined to represent multiple disturbances, including the power disturbances in low-inertia grids, the uncertainty of grid inertia, and unknown nonlinear dynamics. The extended high gain observer is used to estimate the lumped perturbation and the states of the equivalent linear system, which can be further used for the design of the robust feedback controller.
3) The linear quadratic regulator (LQR) is utilized to design the feedback controller. The parameter tuning process is only related to the equivalent linear system, so the controller parameters can be readily tuned and the accurate system models and parameters are not required.

The rest of the paper is organized as follows. In Section II, the nonlinear model of VSC-HVDC systems with the surrounding ac grids. In Section III, the design of the proposed POFFS is elaborated. In Section IV, the stability and robustness of the system with POFFS are elaborated. In Sections V and VI, two case studies are given to verify the effectiveness of the proposed controller. Section VII discusses the influence frequency-dependent dynamics of networks on controller performance. Section VIII concludes the findings of this paper.

## II. System Modeling

The simplified diagram of a VSC-HVDC system connecting a low-inertia grid with the main grid is shown in Fig. 1. AC power drawn from the main grid is converted to dc power by the rectifier station, and is transmitted to the inverter station, which converts the dc power back to ac power to supply the low-inertia grid.

The main grid at the rectifier side is assumed to be an infinite system whose power capacity is far larger than the low-inertia ac grid. The low-inertia ac grid is composed of an aggregated SG, an equivalent load, and a wind farm consists of several doubly fed induction generator (DFIG). Since the frequency stability of the low-inertia grid is mainly determined by the power supply-demand balance, the detailed dynamic models of the renewable energy generator and the load are not required, and the low-inertia grid is simplified as an SG model

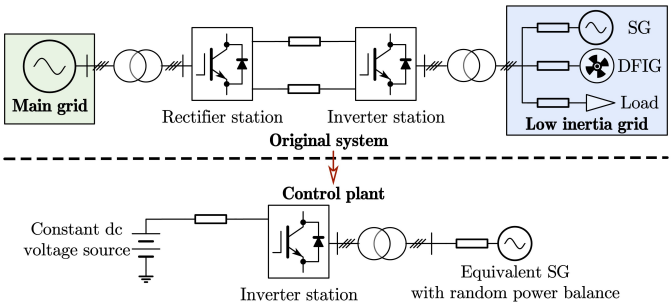


Fig. 1. VSC-HVDC system with low-inertia grid.

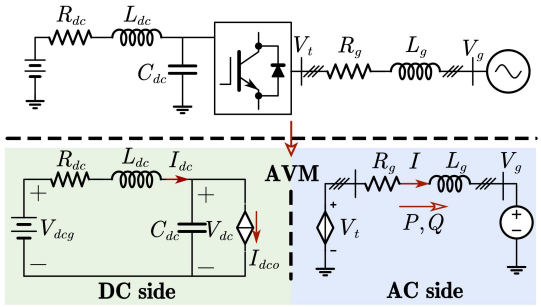


Fig. 2. The diagram of the AVM of the inverter station.

with random power balance. For the VSC-HVDC system, the rectifier station maintains the stability of dc voltage and the inverter station regulates the power injection into the low-inertia grid. Assuming that the performance of the dc voltage controller is good enough, the rectifier stations are simplified as a constant dc voltage source. Consequently, the control plant in this paper is the inverter station with the adjacent ac grid.

### A. Modeling of The Inverter Station

The inverter model is composed of the control system and the VSC model. For the converter model, the average-value model (AVM) is widely used in the analysis of the electromechanical dynamics of VSCs due to the high accuracy and the low calculation burden [31]. The AVM of an inverter station can be modeled by a controlled current source at the dc-side and as a controlled voltage source at the ac-side, as shown in Fig. 2.

Neglecting the switching-losses of VSC-stations, the active power output of VSC-stations $P$ is assumed to be equal to the injected power from the dc network. Thus, the dc dynamics of the inverter station can be represented as

$$\begin{cases} \dot{V}_{dc} = \dfrac{1}{C_{dc}}(I_{dc} - I_{dco}) \\ \dot{I}_{dc} = \dfrac{1}{L_{dc}}(V_{dcg} - V_{dc} - R_{dc}I_{dc}) \\ I_{dco} = \dfrac{P}{V_{dc}} \end{cases} \tag{1}$$

where $C_{dc}$ denotes the equivalent dc-link capacitor of the inverter station; $V_{dc}$ is the dc voltage of the inverter station; $R_{dc}$ and $L_{dc}$ represent the equivalent resistance and inductance of dc transmission lines; $I_{dc}$ is the dc current on the dc cable; $I_{dco}$ are the dc current injected into the converter; $P$ is the active power output of the inverter station.

The ac-side dynamics of the inverter station are modeled in $dq-$reference frame, which are described as

$$\begin{cases} \dot{I}_d = -\dfrac{R_g}{L_g}I_d + \omega I_q + \dfrac{1}{L_g}(V_{td} - V_{gd}) \\ \dot{I}_q = -\dfrac{R_g}{L_g}I_q - \omega I_d + \dfrac{1}{L_g}(V_{tq} - V_{gq}) \\ V_{td} = m_d V_{dc} \\ V_{tq} = m_q V_{dc} \\ P = V_{td}I_d \\ Q = -V_{td}I_q \end{cases} \tag{2}$$

where $V_{td,tq}$ and $I_{d,q}$ are the $d-$ and $q-$axis components of ac voltage and current of the inverter station; $V_{gd}$ and $V_{gq}$ are the $d-$ and $q-$axis components of ac voltage at the PCC; $R_g$ and $L_g$ represent the equivalent resistance and inductance of multiple apparatus, including filters, transformers, and transmission lines; $\omega$ is the angular speed; $m_d$ and $m_q$ are the $d-$ and $q-$axis components of duty cycles.

For the control system of the inverter station, the outer-inner controller and the phase-locked loop (PLL) are often adopted. Fig. 3 shows the structure of the outer-inner controller. The outer controller aims at regulating the power output of converters by generating the $d-$ and $q-$axis current references, which will be tracked by the inner controller rapidly. The dynamics of the outer-inner controller are given as

$$\begin{cases} \dot{P}_f = \dfrac{1}{T_p}(P - P_f) \\ \dot{Q}_f = \dfrac{1}{T_p}(Q - Q_f) \\ \dot{\phi}_P = P_{ref} + P_u - P_f \\ \dot{\phi}_Q = Q_{ref} - Q_f \\ I_{dref} = K_{P1}(P_{ref} + P_u - P_f) + K_{I1}\phi_P \\ I_{qref} = K_{P1}(Q_{ref} - Q_f) + K_{I1}\phi_Q \\ \dot{\gamma}_d = I_{dref} - I_d \\ \dot{\gamma}_q = I_{qref} - I_q \\ m_d = \dfrac{1}{V_{dc}}[-\omega I_q L_g + K_{P2}(I_{dref} - I_d) + K_{I2}\gamma_d] \\ m_q = \dfrac{1}{V_{dc}}[\omega I_d L_g + K_{P2}(I_{qref} - I_q) + K_{I2}\gamma_q] \end{cases} \tag{3}$$

where $P_f$ and $Q_f$ denote the measured active and reactive power of the inverter station; $P_u$ is the additional active power control signal which needs to be designed; $\phi_P$, $\phi_Q$, $\gamma_d$ and $\gamma_q$ are the internal state variables of the proportional-integral (PI) controllers; $K_{P1}$, $K_{P2}$, $K_{I1}$ and $K_{I2}$ are the proportional and integral gains of the PI controllers; $P_{ref}$ and $Q_{ref}$ are the references of power output of VSCs; $I_{dref}$ and $I_{qref}$ are the $dq-$ axis current references.

The PLL is an essential component for the inverter station to synchronize with ac grids. The PLL ensures that the $d-$axis is always aligned with the ac-terminal voltage, i.e., $V_t$. The block diagram of the PLL is shown in Fig. 4 and the dynamics is given as

$$\begin{cases} \dot{x}_{pll} = V_{tq} \\ \dot{\theta} = \omega_0 + K_{P3}V_{tq} + K_{I3}x_{pll} \end{cases} \tag{4}$$

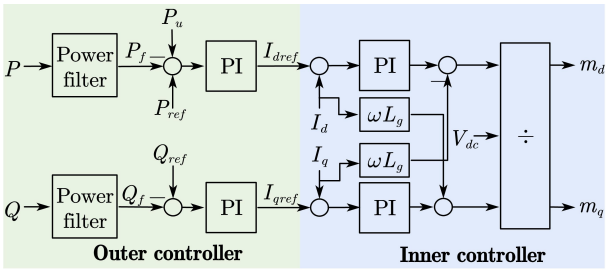


Fig. 3. The block diagram of the double-loop controller.

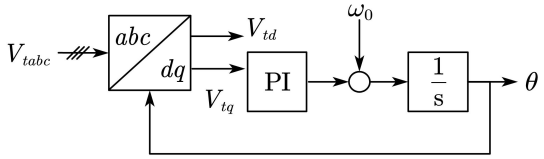


Fig. 4. The block diagram of the PLL.

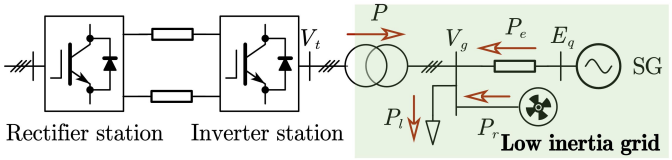


Fig. 5. The signle line diagram of the test system.

where $K_{P3}$ and $K_{I3}$ are the proportional and integral gains of the PI controller; $\omega_0$ is the nominal grid frequency in p.u.; $x_{pll}$ is the internal state variable of the PLL; $\theta$ denotes the phase angle of $V_t$.

### B. Modeling of The Low-Inertia Grid

Fig. 5 shows the simplified ac grid model, which consists of an aggregated synchronous generator (SG), an aggregated load, and a wind generator. The ac grid has the following power balance relationship

$$P_e + P_r + P - P_l = 0 \tag{5}$$

where $P_e$ is the electrical power output of the SG; $P_r$ is the renewable energy generation; $P$ is the power injected by the VSC-HVDC system, and $P_l$ is the power demand.

Eq. (5) indicates that the electrical power output of the generator $P_e$ is reflected instantaneously by the load change of the ac grid, which can lead to the variation of the electrical torque $T_e$ on the rotor and the grid frequency is further influenced because of the torque mismatch on the rotor. The dynamics of grid frequency can be described by a three-order generator model.

$$\begin{cases} \dot{\omega}_g = \dfrac{1}{2H_g}[T_m - T_e - D_g(\omega_g - \omega_0)] \\ \dot{\delta} = \omega_n(\omega_g - \omega_0) \\ \dot{E}'_q = \dfrac{1}{T'_{d0}}(-E_q + E_{fds} + u_f) \end{cases} \tag{6}$$

where $H_g$ and $D_g$ denote the inertia constant and damping coefficient of SGs; $T_m$ and $T_e$ are the mechanical and electrical torque on the SG rotor; $\omega_g$ is the grid frequency in p.u.; $\omega_n$ represents the nominal angular speed in rad/s; $E_q$ is the electric potential of SG; $\delta$ is the phase angle of $E_q$; $E'_q$ is the electric potential behind the transient reactance $X'_d$. $T_m$, $T_e$, $P_e$ and $E_q$ are given by $T_m = \frac{P_m}{\omega_g}, T_e = \frac{P_e}{\omega_g}, P_e = \frac{E_q V_g}{X_d}\sin\delta$, $E_q = \frac{X_d}{X'_d}E'_q - \frac{X_d - X'_d}{X'_d}V_g\cos\delta$.

The aggregated load of the ac grid is represented by the frequency-voltage dependent load model

$$\begin{cases} P_l = P_0[p_1 V_g^2 + p_2 V_g + p_3][1 + K_{pf}(\omega_g - \omega_0)] + P_{ld} \\ Q_l = Q_0[q_1 V_g^2 + q_2 V_g + q_3][1 + K_{qf}(\omega_g - \omega_0)] + Q_{ld} \end{cases} \tag{7}$$

where $P_0$ and $Q_0$ are the initial load power; $p_1 - p_3$ and $q_1 - q_3$ are proportion coefficients of active and reactive power; $K_{pf}$ and $K_{qf}$ are the frequency dependent coefficients of active and reactive power; $P_{ld}$ and $Q_{ld}$ are the random active and reactive power disturbance. This paper mainly focuses on the impact of active power disturbance on system frequency.

SGs are typically required to provide the primary frequency regulation service. The speed governor with a non-reheat turbine is also taken into account.

$$\begin{cases} \dot{T}_m = \dfrac{1}{T_{CH}}(G - T_m) \\ \dot{G} = \dfrac{1}{T_G}(G_0 + K_f(\omega_0 - \omega_g) - G) \end{cases} \tag{8}$$

where $G$ is the valve position; $K_f$ is the droop coefficient of the governor; $T_G$ and $T_{CH}$ denote the time constant of the governor and the steam turbine.

Moreover, a low-pass filter is used to describe the dynamics of the frequency measurement device.

$$\dot{\omega}_m = \frac{1}{T_m}(\omega_g - \omega_m) \tag{9}$$

where $\omega_m$ is the measured frequency; $T_m$ is the time constant.

### C. Completed Nonlinear Model of The Control Plant

The inverter station with the adjacent ac grid is selected to be the completed control plant. The control target is to minimize the frequency deviation of the low-inertia grid by regulating the power output of the inverter station. The disturbances that could lead to frequency excursion include the stochastic load disturbance $P_{ld}$ and the random wind power generation $P_r$, which can be merged into one disturbance term, i.e. $u_d = P_d = P_{ld} - P_r$, and can be regarded as the disturbance input signal. According to the regulation of the power output of the inverter station, the power deficiency of the low-inertia grid and the frequency deviation can be mitigated. Hence the additional power reference of the inverter station is selected as the control input signal, i.e., $u = P_u$, and the output signal is the deviation of the frequency measurement from the nominal value, i.e., $y = \omega_m - \omega_0 = e_\omega$. The nonlinear model of the control plant can be derived from (1)−(9), which are given as

$$\begin{cases} \dot{\mathbf{x}} = \mathbf{f}(\mathbf{x}) + \mathbf{d}(\mathbf{x})u_d + \mathbf{g}(\mathbf{x})u \\ \quad = \mathbf{F}(\mathbf{x}) + \mathbf{g}(\mathbf{x})u \\ y = h(\mathbf{x}) \end{cases} \tag{10}$$

where $\mathbf{f}(\mathbf{x})$, $\mathbf{g}(\mathbf{x})$, and $\mathbf{F}(\mathbf{x})$ are the vector fields, and $\mathbf{F}(\mathbf{x}) = \mathbf{f}(\mathbf{x}) + \mathbf{d}(\mathbf{x})u_d$. $h(\mathbf{x})$ is a scalar function. $\mathbf{x}$ denotes the state vector, which is given by

$$\mathbf{x} = [V_{dc}, I_{dc}, I_d, I_q, P_f, Q_f, \phi_P, \phi_Q, \gamma_d, \gamma_q, x_{pll}, \theta, \omega_g, \delta, E'_q, T_m, G, \omega_m]^T$$

## III. Design of Perturbation Observer-Based Fast Frequency Support Controller of VSC-HVDC

The design of the proposed POFFS controller contains three steps. First, the nonlinear relationship between the frequency excursion $e_\omega$ and the additional power reference of the inverter station $P_u$ is revealed by the input-output feedback linearization technique. Then an exactly input-output linearized model is derived by this relationship and a lumped perturbation is defined to represent the impact of the power disturbances $P_d$ and the unknown system dynamics. Finally, a perturbation observer is designed to estimate the lumped perturbation, and the feedback controller is designed to compensate for the lumped perturbation and to achieve robust frequency regulation.

### A. Feedback Linearization of the Control Plant

The feedback linearization technique is a mature nonlinear control technique. The original nonlinear system can be transformed into the equivalent linear system by state transformation. Hence the linear control techniques can be adopted to design the feedback controller.

Consider the single-input and single-output (SISO) nonlinear system given in (10), the nonlinear relationship between the output signal $y$ and the control input signal $u$ can be obtained by the Lie derivative of the scalar function $h(\mathbf{x})$ with respect to $\mathbf{F}(\mathbf{x})$ and $\mathbf{g}(\mathbf{x})$, which is defined as follows:

$$\begin{cases} L_{\mathbf{F}}h(\mathbf{x}) = \dfrac{\partial h(\mathbf{x})}{\partial \mathbf{x}}\mathbf{F}(\mathbf{x}) \\ L^k_{\mathbf{F}}h(\mathbf{x}) = L_{\mathbf{F}}(L^{k-1}_{\mathbf{F}}h(\mathbf{x})), k = 1, 2, ... \\ L_{\mathbf{g}}h(\mathbf{x}) = \dfrac{\partial h(\mathbf{x})}{\partial \mathbf{x}}\mathbf{g}(\mathbf{x}) \\ L_{\mathbf{g}}L_{\mathbf{F}}h(\mathbf{x}) = \dfrac{\partial L_{\mathbf{F}}h(\mathbf{x})}{\partial \mathbf{x}}\mathbf{g}(\mathbf{x}) \end{cases} \tag{11}$$

Differentiating the output signal $y$ with respect to time until the following conditions are met, i.e.,

$$\begin{cases} L_{\mathbf{g}}L^k_{\mathbf{F}}h(\mathbf{x}) = 0, k = 1, 2, 3, ..., r-2 \\ L_{\mathbf{g}}L^{r-1}_{\mathbf{F}}h(\mathbf{x}) \neq 0 \end{cases} \tag{12}$$

where $r$ is the relative degree between the output and the input signal, which indicates that the input signal $u$ will explicitly appear in the $r$-th derivative of the output signal $y$. Hence, the nonlinear relationship between $u$ and $y$ can be described as

$$y^{(r)} = L^r_{\mathbf{F}}h(\mathbf{x}) + L_{\mathbf{g}}L^{r-1}_{\mathbf{F}}h(\mathbf{x})u \tag{13}$$

The $L^r_{\mathbf{F}}h(\mathbf{x})$ and $L_{\mathbf{g}}L^{r-1}_{\mathbf{F}}h(\mathbf{x})$ in (13) are complicated nonlinear terms, which could be eliminated by the feedback control signal $u$:

$$u = \frac{v - L^r_{\mathbf{F}}h(\mathbf{x})}{L_{\mathbf{g}}L^{r-1}_{\mathbf{F}}h(\mathbf{x})} \tag{14}$$

where $v$ is an additional control input signal.

Substituting (14) into (13) yields

$$y^{(r)} = v \tag{15}$$

As can be observed from (10)−(15), the original system (10) can be simplified as a linear system (15) by the nonlinear feedback controller (14). The dynamic relationship between the output signal $y$ and the additional input signal $v$ is a linear integrator chain. Subsequently, linear control techniques can be utilized to design the additional control input signal $v$ to achieve the reference tracking.

Applying the feedback linearization technique to the inverter station with ac grid described in (10), the first-order Lie derivatives of the frequency deviation $e_\omega$ with respect to $\mathbf{F}(\mathbf{x})$ and $\mathbf{g}(\mathbf{x})$ are given as

$$L_{\mathbf{F}}h(\mathbf{x}) = \frac{\omega_g}{T_m} - \frac{\omega_m}{T_m}, L_{\mathbf{g}}h(\mathbf{x}) = 0 \tag{16}$$

Hence, the first derivative of $\omega_m$ is given by

$$\dot{y} = \dot{e}_\omega = L_{\mathbf{F}}h(\mathbf{x}) = \frac{\omega_g}{T_m} - \frac{\omega_m}{T_m} \tag{17}$$

Since the additional power reference $P_u$ does not appear in (17), the second order derivative of $e_\omega$ needs to be derived.

$$\ddot{e}_\omega = \frac{\dot{\omega}_g}{T_m} - \frac{\dot{\omega}_m}{T_m} = L^2_{\mathbf{F}}h(\mathbf{x}) + L_{\mathbf{g}}L_{\mathbf{F}}h(\mathbf{x})P_u \tag{18}$$

where $L^2_{\mathbf{F}}\mathbf{h}(\mathbf{x})$ and $L_{\mathbf{g}}L_{\mathbf{F}}\mathbf{h}(\mathbf{x})$ are given as

$$\begin{cases} L^2_{\mathbf{F}}h(\mathbf{x}) = \dfrac{P_m}{2H_gT_m\omega_g} - \dfrac{P_d}{2H_gT_m\omega_g} - \dfrac{D_g(\omega_g - \omega_0)}{2H_gT_m} \\ \quad - \dfrac{\omega I_q L_g I_d}{2H_gT_m\omega_g} + \dfrac{K_{I2}\gamma_d I_d}{2H_gT_m\omega_g} - \dfrac{K_{P2}I_d^2}{2H_gT_m\omega_g} \\ \quad + \dfrac{K_{P2}K_{P1}P_{ref}I_d}{2H_gT_m\omega_g} - \dfrac{K_{P2}K_{P1}P_fI_d}{2H_gT_m\omega_g} \\ \quad + \dfrac{K_{P2}K_{I1}\phi_P I_d}{2H_gT_m\omega_g} + \dfrac{I_dV_{gd}}{2H_gT_m\omega_g} \\ \quad - \dfrac{P_0(p_1V_g^2 + p_2V_g + p_3)}{2H_gT_m\omega_g} \\ \quad - \dfrac{P_0K_{pf}[p_1V_g^2 + p_2V_g + p_3](\omega_g - \omega_0)}{2H_gT_m\omega_g} \\ \quad - \dfrac{P_0K_{pf}(\omega_g - \omega_0)}{2H_gT_m\omega_g} - \dfrac{\omega_g - \omega_m}{T_m^2} \\ L_{\mathbf{g}}L_{\mathbf{F}}h(\mathbf{x}) = \dfrac{K_{P2}K_{P1}I_d}{2H_gT_m\omega_g} \end{cases} \tag{19}$$

To cancel the impact of the nonlinear terms on grid frequency, the additional power reference of the inverter station can be designed as

$$P_u = \frac{v - L^2_{\mathbf{F}}h(\mathbf{x})}{L_{\mathbf{g}}L_{\mathbf{F}}h(\mathbf{x})} \tag{20}$$

Substituting (20) into (18) yields

$$\ddot{e}_\omega = v \tag{21}$$

Eq. (21) indicates that the original nonlinear system (10) is transformed into an equivalent linear system (21). Defining

the new state variables i.e., $z_1 = e_\omega$ and $z_2 = \dot{z}_1$, (21) can be rewritten as the state-space format

$$\underbrace{\begin{bmatrix}\dot{z}_1\\ \dot{z}_2\end{bmatrix}}_{\dot{\mathbf{z}}} = \underbrace{\begin{bmatrix}0 & 1\\ 0 & 0\end{bmatrix}}_{\mathbf{A}}\underbrace{\begin{bmatrix}z_1\\ z_2\end{bmatrix}}_{\mathbf{z}} + \underbrace{\begin{bmatrix}0\\ 1\end{bmatrix}}_{\mathbf{B}} v \tag{22}$$

where $\mathbf{z}$ is the state vector, i.e., $\mathbf{z} = [z_1, z_2]^T$; $\mathbf{A}$ and $\mathbf{B}$ are the state and input matrices.

According to the manipulation of the additional input signal $v$, the grid frequency can be regulated. However, as can be observed in (19), $L_{\mathbf{F}}^2\mathbf{h}(\mathbf{x})$ and $L_{\mathbf{g}}L_{\mathbf{F}}\mathbf{h}(\mathbf{x})$ require many system measurements and parameters, which make the controller (20) hard to be applied in real applications. Some of the measurements even can not be measured in real-time, e.g., the accurate random power disturbance $P_d$ occurring in ac grids, the internal state variables of the controller $\phi_P$ and $\gamma_d$. Moreover, some of the system parameters could vary with the operation states, e.g., the inertia time constant $H_g$ and damping coefficient $D_g$ of ac grids. These factors, including unknown system dynamics, parameter uncertainties, and external disturbances, can be treated as system perturbations, which could weaken the controller performance or even threaten the system stability.

### *B. Perturbation Observer-Based Feedback Controller*

In this part, a perturbation observer is designed to estimate the impact of the aforementioned disturbances on grid frequency. Since the disturbances mainly influence the terms $L_{\mathbf{F}}^2 h(\mathbf{x})$ and $L_{\mathbf{g}}L_{\mathbf{F}}h(\mathbf{x})$ in (18), a lumped perturbation term $\Psi$ is defined to represent the impact of these disturbances on system dynamics:

$$\Psi = L_{\mathbf{F}}^2 h(\mathbf{x}) + (L_{\mathbf{g}}L_{\mathbf{F}}h - \beta_0)P_u \tag{23}$$

where $\beta_0$ denotes the nominal value of $L_{\mathbf{g}}L_{\mathbf{F}}h$.

Substituting (23) into (18), (22) can be written as

$$\dot{\mathbf{z}} = \mathbf{A}\mathbf{z} + \mathbf{B}(\Psi + \beta_0 P_u) \tag{24}$$

Similar with (20), the additional power reference is given as

$$P_u = \frac{v - \Psi}{\beta_0} \tag{25}$$

The lumped perturbation term $\Psi$ is assumed to be unknown. To estimate $\Psi$, a new state variable $z_3$ is introduced into the linear system (24) to represent $\Psi$, i.e., $z_3 = \Psi$ and

$$\begin{cases}\dot{z}_1 = z_2\\ \dot{z}_2 = z_3 + \beta_0 P_u\\ \dot{z}_3 = \dot{\Psi}\end{cases} \tag{26}$$

For the extended state system (26), the perturbation observer can be designed on the basis of high gain observer technique. The frequency deviation $e_\omega$ can be obtained from the ac grid. Other state variables, i.e., $z_2$ and $z_3$, are estimated by the perturbation observer, which is described as

$$\begin{cases}\dot{\hat{z}}_1 = \hat{z}_2 + \dfrac{\alpha_1}{\epsilon}(z_1 - \hat{z}_1)\\ \dot{\hat{z}}_2 = \hat{z}_3 + \beta_0 P_u + \dfrac{\alpha_2}{\epsilon^2}(z_1 - \hat{z}_1)\\ \dot{\hat{z}}_3 = \dfrac{\alpha_3}{\epsilon^3}(z_1 - \hat{z}_1)\end{cases} \tag{27}$$

where the superscript '$\hat{}$' denotes the estimate of states; $\epsilon$ is a small positive constant; $\alpha_1 - \alpha_3$ are the observer gains, which could be chosen by pole placement technique such that the polynomials $s^3 + \alpha_1 s^2 + \alpha_2 s + \alpha_3 = 0$ is Hurwitz and the poles of the observer are 10 times faster than the equivalent linear system dynamics. The constant $\epsilon$ is often chosen small enough to ensure the dynamics of the estimation errors converge to zeros quickly. Consequently, the perturbation observer can estimate the dynamics of equivalent linear system and the lumped perturbation in real-time.

With the estimates of state variables $z_1, z_2$ and the lumped perturbation $\Psi$, the impact of perturbations and system nonlinearities can be canceled through the feedback control loop. By designing the additional input signal $v$, i.e., $v = -k_1\hat{z}_1 - k_2\hat{z}_2$, the grid frequency can be stabilized. Consequently, the proposed frequency support controller is given as

$$P_u = \frac{1}{\beta_0}(-\mathbf{K}\hat{\mathbf{z}} - \hat{z}_3) \tag{28}$$

where $\hat{\mathbf{z}} = [\hat{z}_1, \hat{z}_2]^T$; $\mathbf{K}$ is the feedback gain matrix, i.e., $\mathbf{K} = [k_1, k_2]$, which can be obtained by several control techniques, e.g., optimal linear quadratic regulator (LQR), pole placement, etc. In this paper, the LQR is adopted to design $\mathbf{K}$.

To minimize the grid frequency excursion, the following cost function is defined for the equivalent linear system (22):

$$J = \int_0^\infty (\mathbf{z}^T\mathbf{Q}\mathbf{z} + v^T\mathbf{R}v)dt \tag{29}$$

where $\mathbf{Q}$ and $\mathbf{R}$ are the positive-definite weighting matrices. The matrix $\mathbf{Q}$ determines the variation of the state variables, i.e., the frequency deviation and ROCOF, and the matrix $\mathbf{R}$ determines the expenditure of the control energy.

The cost function of the equivalent linear system could be minimized by choosing the appropriate feedback gain matrix $\mathbf{K}$, which can be solved by the Riccati equation

$$\mathbf{A}^T\mathbf{P} + \mathbf{P}\mathbf{A} + \mathbf{Q} - \mathbf{P}\mathbf{B}\mathbf{R}^{-1}\mathbf{B}^T\mathbf{P} = 0 \tag{30}$$

where $\mathbf{P}$ is a symmetric positive definite matrix, which is the solution of the Riccati equation.

Then the feedback gain matrix can be obtianed by

$$\mathbf{K} = \mathbf{R}^{-1}\mathbf{B}^T\mathbf{P} \tag{31}$$

Considering that the inverter station should not operate in overload state, let $P_{u0} = \frac{1}{\beta_0}(-\mathbf{K}\hat{\mathbf{z}} - \hat{z}_3)$ and the following constraints should be considered.

$$P_u = \begin{cases}P_{u,min}, & \text{if } P_{u0} \le P_{u,min}\\ P_{u0}, & \text{if } P_{u,min} \le P_{u0} \le P_{u,max}\\ P_{u,max}, & \text{if } P_{u0} \ge P_{u,max}\end{cases} \tag{32}$$

where $P_{u,max}$ and $P_{u,min}$ are the maximum and minimum power adjustment of the inverter station, which could be determined by the system operator.

The completed diagram of the proposed POFFS controller is shown in Fig. 6, which consists of the perturbation observer (27) and the feedback control law (32). To applied in real power systems, the speed of the center of inertia (COI) is used as the grid frequency, which can be described as

$$\dot{\omega}_g = \frac{\sum H_{gi}\omega_i}{\sum H_{gi}} \tag{33}$$

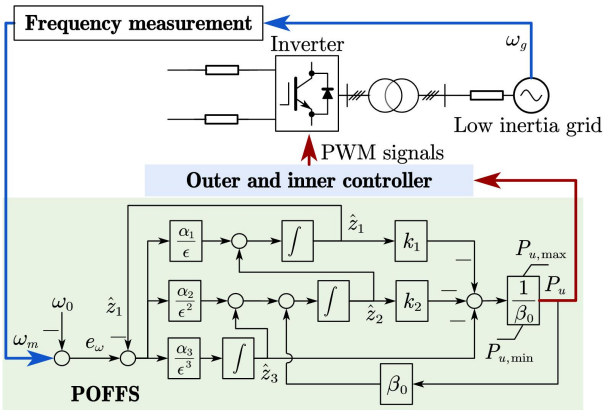


Fig. 6. The block diagram of the propsoed controller.

where $H_{gi}$ and $\omega_i$ are the inertia constant and rotor speed of the $i$-th SG.

After receiving the frequency measurement $\omega_m$, the frequency excursion $e_\omega$ is calculated and the observer estimates the impact of the perturbations and the state variables of the equivalent linear system (22), i.e., $\hat{z}_1 - \hat{z}_3$. Subsequently, the feedback controller utilizes the estimates to calculate the appropriate additional power reference of the inverter station $P_u$ to provide frequency support.

### C. Controller Design Process

The controller design process can be summarized as follows:

1) Use the system nominal parameters to calculate $\beta_0$;
2) Choose the LQR weighting matrices $\mathbf{Q}$ and $\mathbf{R}$, and calculate the optimal feedback gain matrix $\mathbf{K}$ by solving the Riccati equation (30), i.e., $k_1 - k_2$;
3) Calculate the eigenvalues of the closed-loop equivalent linear system $\mathbf{A_c} = \mathbf{A} - \mathbf{BK}$;
4) Select the eigenvalues of the observer gain matrix such that the dynamics of perturbation observer is 5−10 times faster than that of the equivalent linear system;
5) Use the pole placement technique to determine the observer gain matrix, i.e., $\alpha_1 - \alpha_3$;
6) Construct the controller shown in Fig. 6.

## IV. Stability and Robustness Analysis

The stability of the closed-loop system with POFFS is investigated in this section. Define scaled estimation errors

$$\eta_1 = \frac{z_1 - \hat{z}_1}{\epsilon^2}, \eta_2 = \frac{z_2 - \hat{z}_2}{\epsilon}, \eta_3 = z_3 - \hat{z}_3 \tag{34}$$

The observer error can be represented by a singularly perturbed form as

$$\epsilon \cdot \underbrace{\begin{bmatrix}\dot{\eta}_1\\ \dot{\eta}_2\\ \dot{\eta}_3\end{bmatrix}}_{\dot{\eta}} = \underbrace{\begin{bmatrix}-\alpha_1 & 1 & 0\\ -\alpha_2 & 0 & 1\\ -\alpha_3 & 0 & 0\end{bmatrix}}_{\mathbf{A}_\eta} \cdot \underbrace{\begin{bmatrix}\eta_1\\ \eta_2\\ \eta_3\end{bmatrix}}_{\eta} + \epsilon \cdot \underbrace{\begin{bmatrix}0\\ 0\\ 1\end{bmatrix}}_{\mathbf{B}_\eta} \cdot \dot{\Psi} \tag{35}$$

The positive constants $\alpha_1 - \alpha_3$ are chosen such that $\mathbf{A}_\eta$ is a Hurwitzian matrix, and $\epsilon$ is a small constant to be specified in the domain of (0, 1]. Eq. (35) shows that if $\epsilon$ is small enough, the impact of the disturbance $\dot{\Psi}$ could be diminished. Moreover, the dynamics of the estimation error are much faster than that of $\mathbf{z}$.

For the closed-loop system, substituting (28) into (24), the closed-loop system can be obtained as

$$\begin{aligned}\dot{\mathbf{z}} &= \mathbf{Az} + \mathbf{B}(\Psi + \beta_0 P_u)\\ &= \mathbf{Az} + \mathbf{B}(\Psi - \mathbf{K}\hat{\mathbf{z}} - \hat{z}_3)\end{aligned} \tag{36}$$

With the consideration of (34), $\hat{\mathbf{z}}$ can be rewritten as

$$\underbrace{\begin{bmatrix}\hat{z}_1\\ \hat{z}_2\end{bmatrix}}_{\hat{\mathbf{z}}} = \underbrace{\begin{bmatrix}z_1\\ z_2\end{bmatrix}}_{\mathbf{z}} - \underbrace{\begin{bmatrix}\epsilon^2 & 0\\ 0 & \epsilon\end{bmatrix}}_{\mathbf{E}} \cdot \underbrace{\begin{bmatrix}\eta_1\\ \eta_2\end{bmatrix}}_{\eta'} \tag{37}$$

Subtituting (37) into (36) yields

$$\begin{aligned}\dot{\mathbf{z}} &= \mathbf{Az} + \mathbf{B}(\Psi - \mathbf{K}\hat{\mathbf{z}} - \hat{z}_3)\\ &= \mathbf{A_c z} + \mathbf{BKE}\eta' + \mathbf{B}\eta_3\\ &= \mathbf{A_c z} + \mathbf{BK'E'}\eta\end{aligned} \tag{38}$$

where $\mathbf{A_c} = \mathbf{A} - \mathbf{BK}$; $\mathbf{K'} = [\mathbf{K}, 1]$; $\mathbf{E'} = \mathrm{diag}(\mathbf{E}, 1)$. Combined with (35), the closed-loop system can be represented by

$$\dot{\eta} = \frac{1}{\epsilon}\mathbf{A}_\eta \eta + \mathbf{B}_\eta \dot{\Psi} \tag{39}$$

$$\dot{\mathbf{z}} = \mathbf{A_c z} + \mathbf{BK'E'}\eta \tag{40}$$

Assumption 1: The lumped perturbation $\Psi$ and its derivatives $\dot{\Psi}$ in (24) are Lipschitz in their arguments and bounded over the domain of interest.

Assumption 2: The zero dynamics of (24) are exponentially stable and the original operating point is a stable equilibrium point.

A Lyapunov function candidate of the subsystem (39) and (40) is defined as

$$V(z, \eta) = V_z + W_\eta \tag{41}$$

where $V_z = \mathbf{z}^T \mathbf{P_z z}$ , for some $o > 0$, and $\mathbf{P_z}$ is the positive definite solution of Lyapunov equation $\mathbf{P_z A_c} + \mathbf{A_c}^T \mathbf{P_z} = -\mathbf{I_z}$; and $W_\eta = \eta^T \mathbf{P}_\eta \eta$, where $\mathbf{P}_\eta$ is the positive definite solution of Lyapunov equation $\mathbf{P}_\eta \mathbf{A}_\eta + \mathbf{A}_\eta{}^T \mathbf{P}_\eta = -\mathbf{I}_\eta$.

Choose $\xi < o$; then, given Assumption 1, we have, $\forall(\mathbf{z}, \eta) \in B(0, \xi) \times \{(\|\eta\| \le \xi)\} = \Lambda$,

$$|\dot{\Psi}| \le \gamma$$

where $\gamma$ is the upper bound of $\dot{\Psi}$. It can be shown that $\forall(\mathbf{z}, \eta) \in \Lambda$, then, we have

$$\begin{aligned}\dot{V}(\mathbf{z}, \eta) &= \frac{\partial V_z}{\partial \mathbf{z}}\dot{\mathbf{z}} + \frac{\partial W_\eta}{\partial \eta}\dot{\eta}\\ &= \frac{\partial V_z}{\partial \mathbf{z}}(\mathbf{A_c z} + \mathbf{BK'E'}\eta) + \frac{\partial W_\eta}{\partial \eta}(\frac{1}{\epsilon}\mathbf{A}_\eta\eta + \mathbf{B}_\eta\dot{\Psi})\\ &\le -\|\mathbf{z}\|^2 - \frac{1}{\varepsilon}\|\eta\|^2 + 2\|\mathbf{z}\|\|\mathbf{P_z}\|\|\mathbf{BK'}\|\|\mathbf{E'}\|\|\eta\|\\ &\quad + 2\|\eta\|\|\mathbf{P}_\eta\|\gamma\\ &\le -\|\mathbf{z}\|(\|\mathbf{z}\| - 2\|\mathbf{P_z}\|\|\eta\|)\\ &\quad - \|\eta\|(\frac{1}{\epsilon}\|\eta\| - 2\gamma\|\mathbf{P}_\eta\|)\end{aligned} \tag{42}$$

Defining $\xi_2 = 2\epsilon\gamma\|\mathbf{P}_\eta\|$ and $\xi_1 = 2\epsilon\|\mathbf{P}_\mathbf{z}\|\xi_2 = 4\epsilon\gamma\|\mathbf{P}_\eta\|\|\mathbf{P}_\mathbf{z}\|$; Then, for any given $\xi < o$, we can choose

$$\epsilon^* = \min\{\frac{\xi}{8\gamma\|\mathbf{P}_\eta\|\|\mathbf{P}_\mathbf{z}\|}, \frac{\xi}{4\gamma\|\mathbf{P}_\eta\|}\}$$

Then $\forall\epsilon$, $0 < \epsilon < \epsilon^*$, we have $\|\mathbf{z}\| \leq \xi/2$, $\|\eta\| \leq \xi/2$, $\|\mathbf{z}\| \geq \xi_1$, and $\|\eta\| \geq \xi_2$, such that

$$\dot{V}(\mathbf{z},\eta) \leq -\|\mathbf{z}\|(\|\mathbf{z}\| - \xi_1) - \|\eta\|(\|\eta\| - \xi_2) \leq 0 \quad (43)$$

Thus, there is $T(\xi)$ and $T > 0$, it can be shown that

$$\|\mathbf{z}\| + \|\eta\| \leq \xi \quad \forall \geq T \quad (44)$$

The above analysis indicates that the closed-loop systems (39) and estimation error (40) are bounded as long as the Assumptions hold. The lumped perturbation term $\Psi$ considered in this paper includes the impact of the inertia error, model uncertainty, and load demand variation. The grid frequency would not change sharply under these perturbations, because the power system considered in this paper always has inertia. Hence the $\Psi$ and $\dot{\Psi}$ are bounded, continuous, and smooth. According to the perturbation estimation and output feedback control, the proposed POFFS can improve the robustness of the grid frequency to multiple perturbations.

## V. Case Study I

To test the performance of POFFS, the test system with detailed models is developed in DIgSILENT/PowerFactory. The system topology has shown in Fig. 5. The low-inertia grid is composed of a SG, a nonlinear aggregated load, and a wind farm. The SG is represented by the 6-order model with IEEE G1 steam turbine [32] and IEEE type 1 excitation system [33]. The wind farm consists of 25 DFIGs, which are modeled by the built-in 5-MW DFIG model of DIgSILENT. The wind generators are assumed to operate in maximum power point tracking mode, and the inertia or frequency support ability of wind generators is not provided. The nonlinear load is modeled by (7). The parameters of SG and DFIG can be referred to [16]. Other parameters of the test system are given in Table I.

The total load of the ac grid is $P_l = 650$MW, which is supplied by the HVDC ($P = 250$MW), the SG ($P_g = 300$MW), and the wind farm ($P_r = 100$MW). The control performance of POFFS is compared with other five controllers, i.e., $P-\omega$ droop controller, PI-based controller, feedback linearization controller (FLC), VSG, and the extended state observer with linear quadratic regulator (ESOLQR). Three events are considered to test the frequency support performance of these controllers: a)

1) 100MW step load change with parameter uncertainties;
2) Random power generation of the wind farm;
3) 100MW step load change with different grid strength.

### A. Design of POFFS

To minimize the frequency excursion and ROCOF, the LQR weighting matrices $\mathbf{Q}$ and $\mathbf{R}$ are chosen as $\mathbf{Q} = [1000, 0;\ 0, 50]$ and $\mathbf{R} = [1]$. According to (30) and (31), the feedback gain matrix can be calculated as $\mathbf{K} = [31.62, 0; 0, 10.64]$. The eigenvalues of the closed-loop linear system $(\mathbf{A} - \mathbf{BK})$ is $-5.32 \pm j1.82$. To ensure the estimate errors converge to zero quickly, the poles of the perturbation observer are placed at $[-1000, -50 \pm j50]$. According to pole placement technique, the observer gains are calculated as $\alpha_1 = 1100$, $\alpha_2 = 105002$ and $\alpha_3 = 5001510$. The small constant $\epsilon$ is chosen as 0.05. The $\beta_0$ calculated with the nominal parameters is $\beta_0 = 0.166$.

For other five controllers, since the $P-\omega$ droop controller is similar to the primary-frequency regulation of SGs, the droop gain is set to 5 p.u., which is equal to $K_f$ of the SG for identical power sharing. The proportional and integral gains of the PI-based controller are obtained by the Matlab-PI Tunner, which are set to 969 p.u. and 3727 p.u. to achieve a balance between response speed and robustness. The FLC is composed by the (20) and $v = -k_1 e_\omega - k_2 z_1$, where $k_1$ and $k_2$ are the same with POFFS. The important parameters of VSG are virtual inertia and virtual damping coefficient, which are set to 4 s and 5 p.u. The ESOLQR is designed on the basis of the state-space model of (10). The design procedure can refer to [34].

TABLE I
Parameters of the Test System

| |
|---|
| **Inverter station** |
| Rated power: 500MVA, Rated ac voltage: 220kV |
| Rated dc voltage: ± 250kV, short circuit impedance: 15% |
| copper losses: 400kW, no-load losses: 3000kW |
| $R_{dc} = 2.546\Omega$, $L_{dc} = 186.74$mH, $C_{dc} = 0.0005$F |
| $K_{P1} = 2$, $K_{I1} = 10$, $K_{P2} = 1$, $K_{I2} = 500$, $T_m = 50$ms |
| **SG model** |
| Rated power: 600MVA, $H_g = 4$s, $D_g = 1$p.u., $K_f = 5$p.u., $T_G = 0.2$s, $T_{CH} = 0.3$s $R_g = 0.52\Omega$, $L_g = 26.42mH$ |
| **Load** |
| $p_1 = 0.4$, $p_2 = 0.3$, $p_3 = 0.3$, $K_{pf} = K_{qf} = 0.5$p.u. |

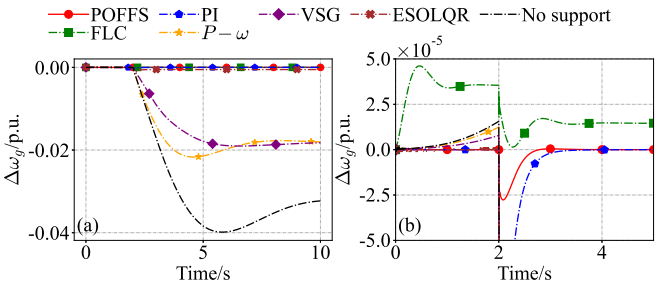


Fig. 7. The grid frequency : (a) complete plot, and (b) enlarged plot.

### B. Step Load Change With Parameter Error

A 100MW step load change event occurs at $t = 2$s. To test the robustness of POFFS, an error of the inertia constant of the low-inertia grid is considered, i.e., $\Delta H_g = 2s$, which means that the $H_g$ is assumed to be 6s when designing the controller but the real inertia of the grid is only 4s. The frequency of the low-inertia gird with different controllers are shown in Figs. 7 – 9.

It can be observed from the black curve in Fig. 7(a) that the sudden change of load demand can lead to large frequency excursion when only the SG provides frequency support. $P-\omega$

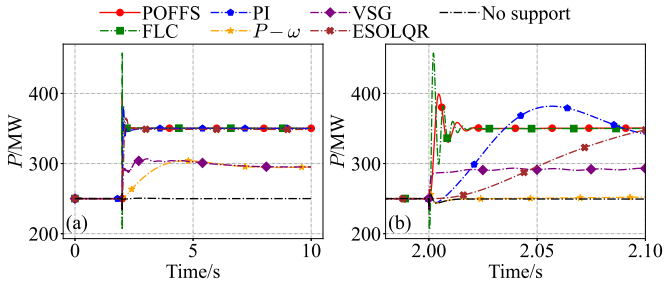


Fig. 8. The power output of the inverter station: (a) complete plot, and (b) enlarged plot.

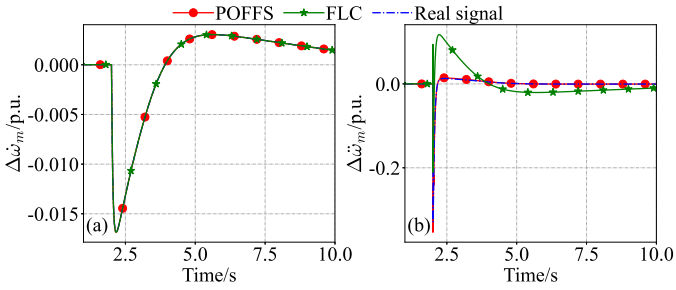


Fig. 9. Derivatives of grid frequency estimated by different controllers: (a) first derivative of grid frequency, and (b) second derivative of grid frequency.

droop controller can somewhat provide frequency support, but the frequency deviation cannot be eliminated [see the orange curve]. VSG has similar steady-state performance with $P-\omega$ droop controller whereas the ROCOF is much lower due to the provision of virtual inertia [see the purple curve]. Both POFFS, FLC, PI, and ESOLQR have satisfying frequency support performance compared with $P-\omega$ droop controller and VSG. It can be observed from 7(b) that POFFS has the best frequency regulation ability among these controllers [see the red curve]. Both the ROCOF and frequency nadir are restrained rapidly, and the frequency can return to the nominal value within 1s. Although FLC can also mitigate the frequency deviation, it could lead to steady-state error due to the inaccurate $H_g$ and the unknown dynamics, e.g., PLL and detailed SG. The PI controller has larger frequency nadir than POFFS [see the blue curve]. ESOLQR can also achieve the satisfying frequency support performance whereas the linear observer will results in steady-state frequency error [see a brown curve in Fig. 7(a)].

The power output of the inverter station with different controllers is shown in Fig. 8, which indicates that the POFFS and FLC can rapidly increase the power output to compensate for the power deficiency of the low-inertia grid. Whilst the other four controllers has relatively slow responses for frequency support.

The estimates of the frequency dynamics are shown in Fig. 9, which indicates that the POFFS can estimate the first and second derivative of frequency measurement accurately, whereas the calculation of the second derivative of frequency by FLC has a greater error due to the unmodeled system dynamics, so the steady-state frequency deviation exists whereas POFFS can recover the frequency to the nominal value.

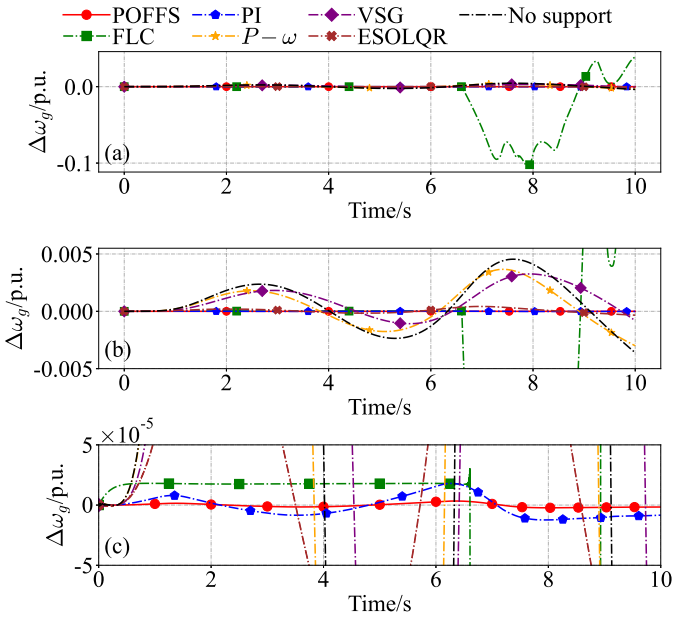


Fig. 10. Grid frequency under the random wind speed: (a) complete plot, (b) enlarged plot, and (c) enlarged plot.

### C. Random Wind Power Generation

The power generation of the wind farm in the ac grid could fluctuate due to the variation in wind speed. To test the robustness of the POFFS, the wind power generation changes within the range of 80−125MW. The frequency responses of the ac gird are shown in Fig. 10.

Since the DFIG dynamics are not taken into account when designing the FLC, FLC will lead to instability due to the unknown system dynamics [see the green curve in Fig. 10(a)]. Fig. 10(b) is the enlarged drawing of Fig. 10(a), which indicates that, except for FLC, both controllers can restrain the frequency variation to some extent. Among these controllers, the proposed POFFS has the best frequency support performance, as shown by the red curve in Fig. 10(c). The grid frequency is very close to its nominal value when POFFS is applied.

### D. Step Load Change With Different Grid-Strength

To test the performance of POFFS under different grid strength, the 100MW-load change event occurs in the ac grid with different short-circuit ratios (SCR), which is often used to describe the grid strength [35]

$$SCR = \frac{S_{ac}}{P_{dn}} = \frac{1}{X_g} \tag{45}$$

where $S_{ac}$ is the short-circuit capacity of the ac grid; $P_{dn}$ is the rated power of the VSC-HVDC system; $X_g$ is per-unit grid impedance based on $P_{dn}$.

An ac grid whose SCR value is lower than 2 can be considered a weak grid. In this section, the POFFS is tested in the ac grid whose SCR value is changed from 1.5 to 4.5. The corresponding $X_g$ is set to 21.51−64.53 Ω. The simulation results are shown in Fig. 11.

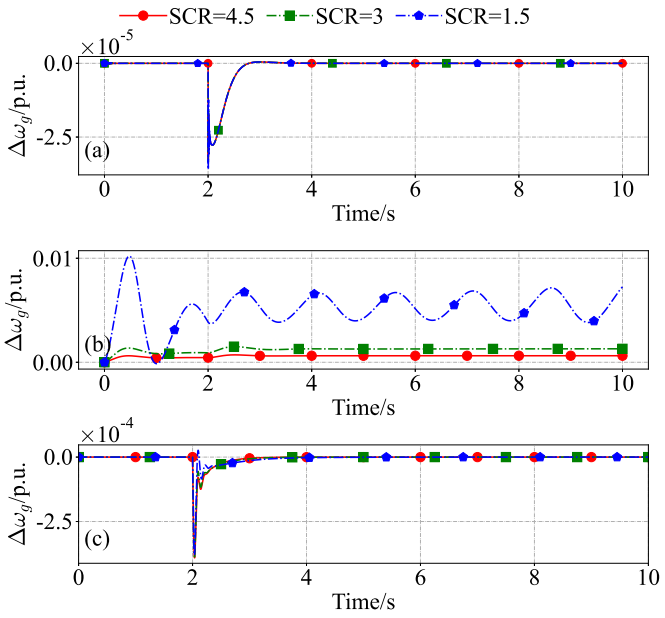


Fig. 11. Grid frequency under the different SCR: (a) POFFS, (b) FLC, and (c) PI.

It can be observed from Fig. 11(a) that the grid-strength has little impact on the frequency support performance of POFFS. Fig. 11(b) indicates that when FLC is applied in the inverter station, the frequency deviation is increased with the reduction of grid strength. The FLC will lead to instability when the VSC-HVDC connects to the very weak grid [SCR $=$ 1.5], as shown by Fig. 11(b). The PI controller also has good frequency support performance whereas the frequency deviation in the supporting process is larger than that when POFFS is applied, as shown by Fig. 11(c). Consequently, the POFFS can achieve the satisfying frequency support under different grid strength.

## VI. Case Study II

To test the robustness control performance of POFFS in multi-machine power systems, the VSC-HVDC system is connected with the IEEE 39-bus system via Bus 39. The rated capacity of the inverter station is modified to 800MVA. The outage of G10 at $t = 2$s is used as the disturbance event with different penetration of wind power. G3$-$G6 are replaced by wind farms, as shown in Table II. To quantify the overall system equivalent inertia level, the following equation is adopted [36]

$$H_g = \frac{\sum_{i=1}^{m} H_{gi} S_{gi}}{\sum_{i=1}^{m} S_{gi} + \sum_{j=1}^{n} S_{rj}} \tag{46}$$

where $m$ is the number of SGs and $n$ is the number of renewable generators; $H_{gi}$ is the inertia constant of the $i$-th SG; $S_{gi}$ and $S_{ri}$ are the rated power capacity of the $i$-th SG and the $j$-th renewable generator, respectively.

### A. Generator Outage Event With Different Penetration of Wind Generation

In this subsection, the ESOLQR and FLC can not work properly due to the significant modeling error, which can lead to the instability of the whole power system. Hence, the performance of the proposed POFFS is only compared with the $P-\omega$, PI, and VSG controllers. The proportional and integral gains of the PI-based controller are set to 152 p.u. and 812 p.u. The parameters of POFFS and other controllers are the same as that in Section IV. The grid frequency responses under

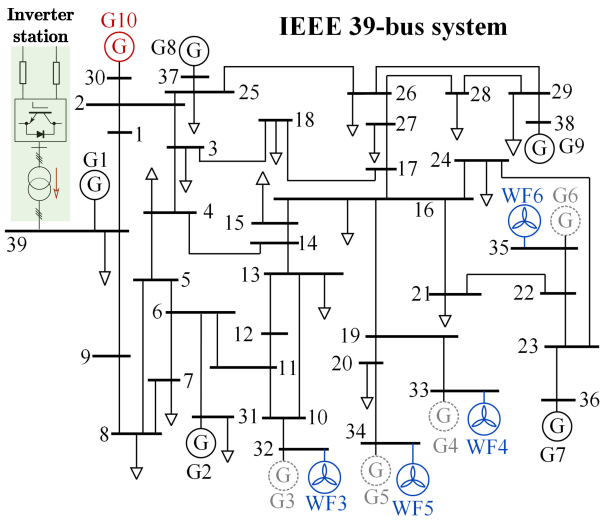


Fig. 12. The single line diagram of the test system.

TABLE II
Penetration of Wind Generation

| SGs to be replaced | - | G3, G4 | G3$-$G5 | G3$-$G6 |
|---|---|---|---|---|
| Percentage of wind power | 0% | 24% | 33% | 45% |
| System inertia | 4.577s | 4.200s | 4.048s | 3.845s |

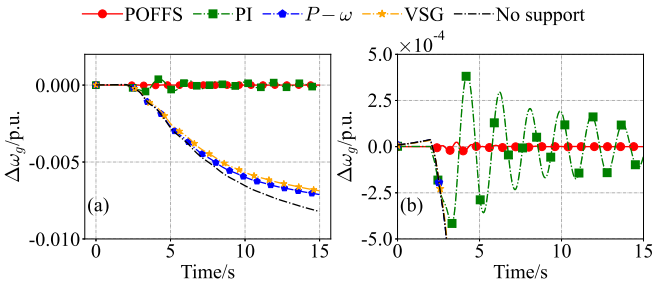


Fig. 13. The grid frequency with 24% wind generation: (a) complete plot, and (b) enlarged plot.

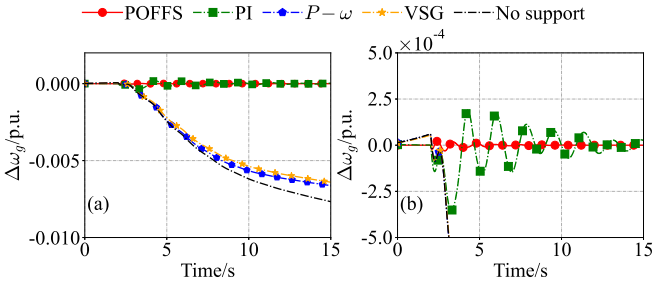


Fig. 14. The grid frequency with 33% wind generation: (a) complete plot, and (b) enlarged plot.

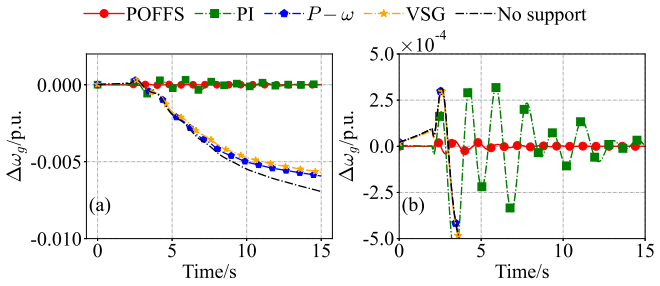


Fig. 15. The grid frequency with 45% wind generation: (a) complete plot, and (b) enlarged plot.

the outage event are shown in Figs. 13 – 15, and the power output of the inverter station is shown in Figs. 16 – 18.

As can be observed from Figs. 13 – 15, the proposed POFFS has the best frequency support performance under the different percentages of wind generation [see the red curves in these figures]. The grid frequency is slightly influenced by the outage of generator G10. The PI controller can also achieve a satisfying frequency support performance, but the oscillation period is longer than POFFS. The $P-\omega$ droop controller and VSG has large steady-state frequency error.

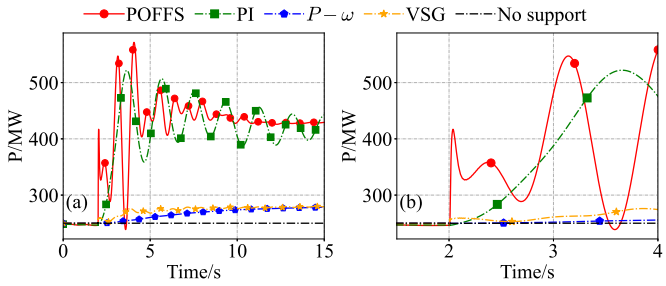


Fig. 16. The power output of the inverter with 24% wind generation: (a) complete plot, and (b) enlarged plot.

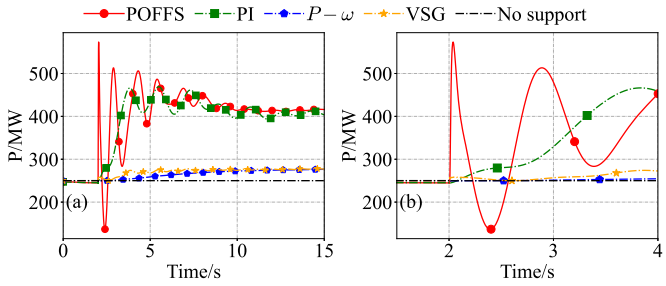


Fig. 17. The power output of the inverter with 33% wind generation: (a) complete plot, and (b) enlarged plot.

The red curves in Figs. 16 – 18 illustrates that POFFS can adjust the power output of the inverter station rapidly to compensate for the power deficiency caused by the outage of G10. At the beginning of the support process, the power oscillations can be observed because the outage of G10 not only triggers the frequency deviation but also the frequency oscillation, which results in the power output oscillation of the inverter station. The PI controller can also provide active

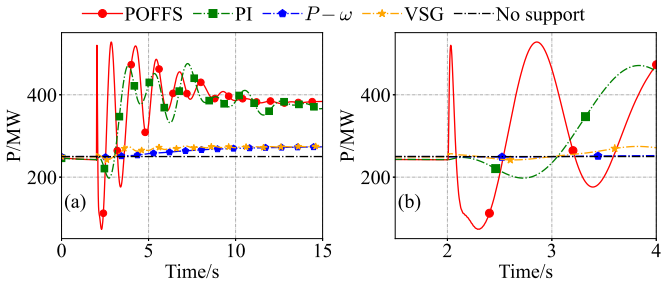


Fig. 18. The power output of the inverter with 45% wind generation: (a) complete plot, and (b) enlarged plot.

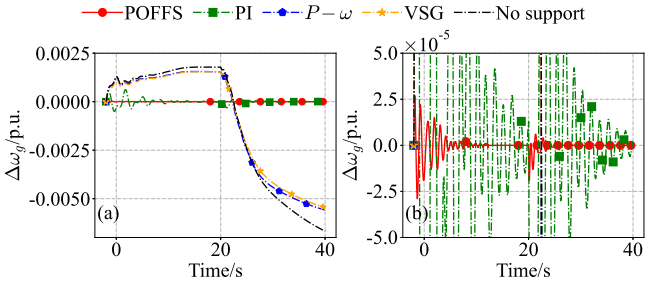


Fig. 19. The grid frequency response: (a) complete plot, and (b) enlarged plot.

power support to the ac grid [see the green curves in Figs. 16 – 18]. However, the regulation speed of the PI controller is relatively slower than POFFS and the oscillations could last for a long time. The blue and yellow curves in Figs. 16 – 18 indicate that the power adjustment of $P-\omega$ droop controller and VSG is proportional to the frequency deviation to realize a certain power-sharing ratio between the inverter station and SGs. Hence POFFS has the best frequency support performance among these controllers.

### *B. Generator Outage Event with the Frequency-Dependent Dynamics of Networks*

In this subsection, the proposed POFFS is tested with the consideration of frequency-dependent dynamics of networks. The outage of G10 at $t = 20$s is used as the disturbance event with 24% penetration of wind generation. The distributed parameter model is used to modeling the transmission lines and the EMT simulation is performed in PowerFactory [37]. The ESOLQR and FLC still can not work properly in this scenario, and the performance of the proposed POFFS is only compared with the $P-\omega$, PI, and VSG controllers. The grid frequency responses and the power output of the inverter station are shown in Figs. 19 and 20.

As can be observed from Figs. 19 and 20, an interesting phenomenon can be observed when the frequency-dependent transmission line model is considered. As shown by the black dashed curve in Fig. 19, the initial operation point is not a balanced point anymore. If the frequency support controllers of the inverter station are not activated, the grid frequency would soar at the beginning of the simulation and would decrease when G10 is out of service at $t = 20$s.

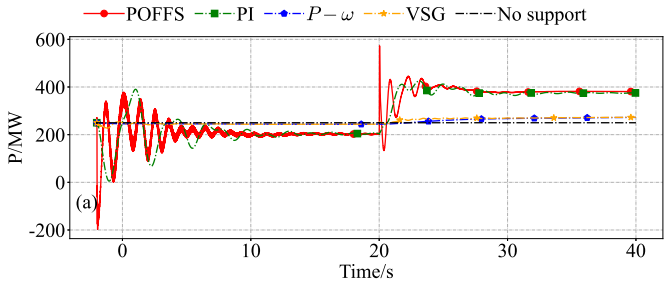


Fig. 20. The power output of the inverter.

If the VSG or $P-\omega$ controller is activated, as shown by the blue and yellow curves in Fig. 19, the frequency deviation could be slightly mitigated due to the weak power regulation capability [see the blue and yellow curves in Fig. 20].

Both the POFFS and the PI controllers can provide satisfied frequency capability, as shown by the red and green curves in Fig. 19. The frequency slightly fluctuates around the nominal value. It can be observed that the proposed POFFS has the best frequency regulation performance. The frequency deviation at the beginning of the simulation and after the outage of G10 is limited in a very narrow range, and converge to zero quickly, since the rapid power regulation of the active power output of the inverter station [see the red curve in Fig. 20].

Consequently, although the distributed parameter model of the transmission lines could affect the dynamics of the network, the proposed POFFS still can achieve a satisfying control performance.

## VII. Discussion

The frequency-dependent dynamics of networks can lead to the variation of the system damping because the frequency-dependent dynamics could change the transfer functions of the system. However, the unknown dynamics of networks can also be regarded as a sort of disturbance, which can be integrated into the lumped perturbation and be estimated by the proposed POFFS. Consequently, the proposed POFFS can also provide a satisfied frequency regulation performance when the frequency-dependent dynamics of networks are considered.

## VIII. Conclusion

This paper has proposed a perturbation observer-based fast frequency support (POFFS) control to improve the frequency stability of low-inertia grids via VSC-HVDC systems. The effectiveness of POFFS is validated by the time-domain simulations. The main conclusions are summarized as follows:

1) The active power reference of the inverter station and the grid frequency has a second-order differential relationship, which helps to simplify the original nonlinear system into an equivalent linear system by feedback linearization technique and facilitates the controller design.
2) Based on the equivalent linear system, the perturbation observer can accurately estimate the comprehensive impact of multiple perturbations on grid frequency, including the power disturbances in low-inertia grids, the uncertainty of grid inertia, and unknown frequency-dependent dynamics of the network. Consequently, POFFS can provide a better robust frequency support performance compared with the conventional FLC, PI-based controller, VSG, and the linear extended state observer-based controller.
3) The structure and parameters of POFFS are determined by the equivalent linear system and the control target, which have little relationship with the internal state variables of the original plant model. Hence the design of the controller and the tuning process are much easier than the classical FLC, PI-based controller, linear extended state observer-based controller, and so on.

## References

[1] G. Tang, Z. Xu, and Y. Zhou, "Impacts of three mmc-hvdc configurations on ac system stability under dc line faults," *IEEE Transactions on Power Systems*, vol. 29, no. 6, pp. 3030–3040, 2014.
[2] K. S. Ratnam, K. Palanisamy, and G. Yang, "Future low-inertia power systems: Requirements, issues, and solutions - a review," *Renewable and Sustainable Energy Reviews*, vol. 124, p. 109773, 2020.
[3] J. Bialek, "What does the gb power outage on 9 august 2019 tell us about the current state of decarbonised power systems?" *Energy Policy*, vol. 146, p. 111821, 2020.
[4] Y. Xue and Z. Xu, "On the bipolar mmc-hvdc topology suitable for bulk power overhead line transmission: Configuration, control, and dc fault analysis," *IEEE Transactions on Power Delivery*, vol. 29, no. 6, pp. 2420–2429, 2014.
[5] Y. Phulpin, "Communication-free inertia and frequency control for wind generators connected by an hvdc-link," *IEEE Transactions on Power Systems*, vol. 27, no. 2, pp. 1136–1137, 2012.
[6] M. M. Kabsha and Z. H. Rather, "A new control scheme for fast frequency support from hvdc connected offshore wind farm in low-inertia system," *IEEE Transactions on Sustainable Energy*, vol. 11, no. 3, pp. 1829–1837, 2020.
[7] Z. Lu, Y. Ye, and Y. Qiao, "An adaptive frequency regulation method with grid-friendly restoration for vsc-hvdc integrated offshore wind farms," *IEEE Transactions on Power Systems*, vol. 34, no. 5, pp. 3582–3593, 2019.
[8] Y. Ye, Y. Qiao, L. Xie, and Z. Lu, "A comprehensive power flow approach for multi-terminal vsc-hvdc system considering cross-regional primary frequency responses," *Journal of Modern Power Systems and Clean Energy*, vol. 8, no. 2, pp. 238–248, 2020.
[9] W. Wang, X. Yin, Y. Cao, L. Jiang, and Y. Li, "A distributed cooperative control based on consensus protocol for vsc-mtdc systems," *IEEE Transactions on Power Systems*, vol. 36, no. 4, pp. 2877–2890, 2021.
[10] S. G. Vennelaganti and N. R. Chaudhuri, "Selective power routing in MTDC grids for inertial and primary frequency support," *IEEE Transactions on Power Systems*, vol. 33, no. 6, pp. 7020–7030, 2018.
[11] M. Zhang, X. Yuan, and J. Hu, "Inertia and primary frequency provisions of pll-synchronized vsc hvdc when attached to islanded ac system," *IEEE Transactions on Power Systems*, vol. 33, no. 4, pp. 4179–4188, 2018.
[12] R. H. Lasseter, Z. Chen, and D. Pattabiraman, "Grid-Forming Inverters: A Critical Asset for the Power Grid," *IEEE Journal of Emerging and Selected Topics in Power Electronics*, vol. 8, no. 2, pp. 925–935, 2020.
[13] D. Pan, X. Wang, F. Liu, and R. Shi, "Transient Stability of Voltage-Source Converters with Grid-Forming Control: A Design-Oriented Study," *IEEE Journal of Emerging and Selected Topics in Power Electronics*, vol. 8, no. 2, pp. 1019–1033, 2020.
[14] Y. Hirase, K. Sugimoto, K. Sakimoto, and T. Ise, "Analysis of resonance in microgrids and effects of system frequency stabilization using a virtual synchronous generator," *IEEE Journal of Emerging and Selected Topics in Power Electronics*, vol. 4, no. 4, pp. 1287–1298, 2016.
[15] A. Tayyebi, D. Grob, A. Anta, F. Kupzog, and F. Dorfler, "Frequency Stability of Synchronous Machines and Grid-Forming Power Converters," *IEEE Journal of Emerging and Selected Topics in Power Electronics*, vol. 8, no. 2, pp. 1004–1018, 2020.
[16] W. Wang, L. Jiang, Y. Cao, and Y. Li, "A parameter alternating vsg controller of vsc-mtdc systems for low frequency oscillation damping," *IEEE Transactions on Power Systems*, vol. 35, no. 6, pp. 4609–4621, 2020.

[17] M. Chen, D. Zhou, and F. Blaabjerg, "Enhanced Transient Angle Stability Control of Grid-Forming Converter Based on Virtual Synchronous Generator," *IEEE Transactions on Industrial Electronics*, vol. 69, no. 9, pp. 9133–9144, 2022.
[18] L. M. Castro and E. Acha, "On the provision of frequency regulation in low inertia ac grids using hvdc systems," *IEEE Transactions on Smart Grid*, vol. 7, no. 6, pp. 2680–2690, 2016.
[19] J. Kaur and N. R. Chaudhuri, "Secondary frequency support to weak grids through coordinating control of hybrid hvdc system," *IEEE Transactions on Power Delivery*, vol. 35, no. 4, pp. 1685–1694, 2020.
[20] L. Jiang, W. Yao, Q. H. Wu, J. Y. Wen, and S. J. Cheng, "Delay-dependent stability for load frequency control with constant and time-varying delays," *IEEE Transactions on Power Systems*, vol. 27, no. 2, pp. 932–941, 2012.
[21] C.-K. Zhang, L. Jiang, Q. H. Wu, Y. He, and M. Wu, "Delay-dependent robust load frequency control for time delay power systems," *IEEE Transactions on Power Systems*, vol. 28, no. 3, pp. 2192–2201, 2013.
[22] F. Yang, J. He, and D. Wang, "New stability criteria of delayed load frequency control systems via infinite-series-based inequality," *IEEE Transactions on Industrial Informatics*, vol. 14, no. 1, pp. 231–240, 2018.
[23] X.-C. Shangguan, C.-K. Zhang, Y. He, L. Jin, L. Jiang, J. W. Spencer, and M. Wu, "Robust load frequency control for power system considering transmission delay and sampling period," *IEEE Transactions on Industrial Informatics*, vol. 17, no. 8, pp. 5292–5303, 2021.
[24] K. Shi, X. Yin, L. Jiang, Y. Liu, Y. Hu, and H. Wen, "Perturbation estimation based nonlinear adaptive power decoupling control for dfig wind turbine," *IEEE Transactions on Power Electronics*, vol. 35, no. 1, pp. 319–333, 2020.
[25] H. Bevrani, M. R. Feizi, and S. Ataee, "Robust frequency control in an islanded microgrid: $h\infty$ and $\mu$ synthesis approaches," *IEEE Transactions on Smart Grid*, vol. 7, no. 2, pp. 706–717, 2016.
[26] C. Peng, J. Li, and M. Fei, "Resilient event-triggering $h_\infty$ load frequency control for multi-area power systems with energy-limited dos attacks," *IEEE Transactions on Power Systems*, vol. 32, no. 5, pp. 4110–4118, 2017.
[27] J. Liu, Y. Gu, L. Zha, Y. Liu, and J. Cao, "Event-triggered $h_\infty$ load frequency control for multiarea power systems under hybrid cyber attacks," *IEEE Transactions on Systems, Man, and Cybernetics: Systems*, vol. 49, no. 8, pp. 1665–1678, 2019.
[28] B. Yang, T. Yu, H. Shu, D. Zhu, N. An, Y. Sang, and L. Jiang, "Perturbation observer based fractional-order sliding-mode controller for mppt of grid-connected pv inverters: Design and real-time implementation," *Control Engineering Practice*, vol. 79, pp. 105–125, 2018.
[29] B. Yang, T. Yu, H. Shu, J. Dong, and L. Jiang, "Robust sliding-mode control of wind energy conversion systems for optimal power extraction via nonlinear perturbation observers," *Applied Energy*, vol. 210, pp. 711–723, 2018.
[30] J. Chen, W. Yao, Y. Ren, R. Wang, L. Zhang, and L. Jiang, "Nonlinear adaptive speed control of a permanent magnet synchronous motor: A perturbation estimation approach," *Control Engineering Practice*, vol. 85, pp. 163–175, 2019.
[31] A. E. Leon and J. M. Mauricio, "Mitigation of subsynchronous control interactions using multi-terminal dc systems," *IEEE Transactions on Sustainable Energy*, vol. 12, no. 1, pp. 420–429, 2021.
[32] P. Pourbeik, G. Chown, J. Feltes, F. Modau, S. Sterpu, R. Boyer, K. Chan, L. Hannett, D. Leonard, L. Lima, W. Hofbauer, L. Gerin-Lajoie, S. Patterson, J. Undrill, and F. Langenbacher, "Dynamic models for turbine-governors in power system studies," *IEEE Power & Energy Society*, 2013.
[33] "Ieee recommended practice for excitation system models for power system stability studies," *IEEE Std 421.5-2016 (Revision of IEEE Std 421.5-2005)*, 2016.
[34] S. Li, J. Yang, W.-H. Chen and X. Chen, *Disturbance Observer-Based Control: Methods and Applications*, 1st ed. London: CRC Press, 2014.
[35] A. Egea-Alvarez, S. Fekriasl, F. Hassan, and O. Gomis-Bellmunt, "Advanced Vector Control for Voltage Source Converters Connected to Weak Grids," *IEEE Transactions on Power Systems*, vol. 30, no. 6, pp. 3072–3081, 2015.
[36] P. Tielens and D. Van Hertem, "The relevance of inertia in power systems," *Renewable and Sustainable Energy Reviews*, vol. 55, pp. 999–1009.
[37] *PowerFactory Technical Reference: Overhead Line Models*, Online edition ed. Gomaringen, Germany: DIgSILENT Gmbh, 2022.